

1 Long-term observations of black carbon and carbon monoxide in the 2 Poker Flat Research Range, central Alaska, with a focus on forest 3 wildfire emissions

4 Takeshi Kinase¹, Fumikazu Taketani^{1,2}, Masayuki Takigawa¹, Chunmao Zhu², Yongwon Kim³, Petr
5 Mordovskoi¹, and Yugo Kanaya^{1,2}

6 ¹Institute of Arctic Climate and Environment Research, Japan Agency for Marine-Earth Science and Technology (JAMSTEC),
7 Yokohama 2360001, Japan

8 ²Earth Surface System Research Center, Research Institute for Global Change, Japan Agency for Marine-Earth Science and
9 Technology (JAMSTEC), Yokohama 2360001, Japan

10 ³International Arctic Research Center, University of Alaska Fairbanks (UAF), Fairbanks 757340, U.S.A.

11

12 *Correspondence to:* Takeshi Kinase (tkinase@jamstec.go.jp)

13 Abstract

14 Forest wildfires in interior Alaska represent an important black carbon (BC) source for the Arctic and sub-Arctic. However,
15 BC observations in interior Alaska have not been sufficient to constrain the range of existing emissions. Here, we show our
16 observations of BC mass concentrations and carbon monoxide (CO) mixing ratios in the Poker Flat Research Range (65.12°
17 N, 147.43° W), located in central Alaska, from April 2016 to December 2020. The medians, 10th, and 90th percentile ranges
18 of the hourly BC mass concentration and CO mixing ratio throughout the observation period were 13, 2.9, and 56 ng m⁻³ and
19 124.7, 98.7, and 148.3 ppb, respectively. Sporadically large peaks in the BC mass concentration and CO mixing ratio were
20 observed at the same time, indicating influences from common sources. These BC peaks coincided with peaks at other
21 comparative sites in Alaska, indicating large BC emissions in interior Alaska. Source estimation by FLEXPART-WRF
22 confirmed a contribution of boreal forest wildfires in Alaska and western Canada when high BC mass concentrations were
23 observed. For these cases, we found a positive correlation ($r = 0.44$) between the observed BC/ Δ CO ratio and fire radiative
24 power (FRP) observed in Alaska and Canada. This finding implies that the variability of the BC and CO emission ratio is
25 associated with the intensity and time progress of forest wildfires and suggests the BC emission factor and/or inventory could
26 be potentially improved by FRP. We recommend that FRP be integrated into future bottom-up emission inventories to achieve
27 a better understanding of the dynamics of pollutants from frequently occurring forest wildfires under the rapidly changing
28 climate in the Arctic.

29

30 **1 Introduction**

31 Climate change in the Arctic region has been strongly accelerated compared to the global average (Box et al., 2019; Bonfils et
32 al., 2020). The near-surface air temperature increased between 1.8 and 3.1 °C in the period between 1971 and 2017 (Box et
33 al., 2019). This rapid temperature increase in the Arctic region caused decreases in the extent of sea ice (Aizawa et al., 2021),
34 resulting in the acceleration of Arctic warming (Cohen et al., 2014; Thackeray and Hall, 2019). Even if net CO₂ emission is
35 controlled to zero until the end of the 21st century (SSP1-2.6 scenario), modelling studies predicted a more than 3.5 °C
36 temperature increase (Cai et al., 2021; Xie et al., 2022). However, there are still some difficulties associated with climate
37 predictions based on global climate models because of the widespread use of different model hindcasts and forecasts (Overland
38 et al., 2014). Specifically, it is known that the Arctic amplification process causes an acceleration in Arctic warming, but the
39 process is highly complicated and is not sufficiently understood; this includes processes involved in aerosol concentration
40 changes and the deposition of black carbon (BC) on snow and ice surfaces (Cohen et al., 2014). Thus, more research is required
41 to understand Arctic climatic processes.

42 BC aerosols, which are formed by various incomplete combustion processes, such as fossil fuel and biomass burning (Bond et
43 al., 2013), strongly contribute to warming by absorbing solar radiation (Bond et al., 2013; IPCC, 2021). In addition, BC
44 deposited on snow and ice surfaces decreases surface albedo and contributes to snow melting and warming (Aoki et al., 2011;
45 Bond et al., 2013; Oshima et al., 2020; IPCC, 2021). BC can be transported over long distances (estimated lifetimes are 3–6
46 days globally (Wang et al., 2014; Lund et al., 2018)) and affect the climate and environment of remote regions, such as the
47 Arctic (Wang et al., 2011; Matsui et al., 2022). However, large discrepancies among model estimations for BC climate effects
48 on the Arctic remain (Gliß et al., 2021) because of a lack of observation data (IPCC, 2021) to constrain the models in terms of
49 dependence on emission inventories (Pan et al., 2020; Matsui et al., 2022) and/or removal rates (Ikeda et al., 2017; Lund et al.,
50 2018). For long-range transport from Asia to the Arctic, constraints on the major BC emissions from East Asia (Choi et al.,
51 2020; Kanaya et al., 2020), ship-based observations for BC transport to the Arctic (Taketani et al., 2016, 2022), evaluation of
52 the multimodel bias using these datasets (Whaley et al., 2022) and an improved understanding of transport mechanisms and
53 source attributions (Ikeda et al., 2017; Zhu et al., 2020) have been achieved. However, more observational constraints are
54 required for the characterization of BC emissions from boreal forest wildfires (Pan et al., 2020; AMAP, 2021).

55 Forest wildfires in the northern American region, especially those that occur in Alaska every summer (Picotte et al., 2020), are
56 one of the important BC emission sources in the Arctic and subarctic troposphere, and they result in depositional fluxes on
57 snow and ice over the Arctic and surrounding regions (Xu et al., 2017; AMAP, 2021; Matsui et al., 2022). The occurrences of
58 these forest wildfires in interior Alaska have increased since the 1980s (Sierra-Hernández et al., 2022), and this increasing
59 trend is predicted to continue (Hu et al., 2015; Box et al., 2019; AMAP, 2021); the emission of aerosols, including BC from
60 forest wildfires, is projected to severely affect the environment (Halofsky et al., 2020) and climate (Schmale et al., 2021) in
61 the future.

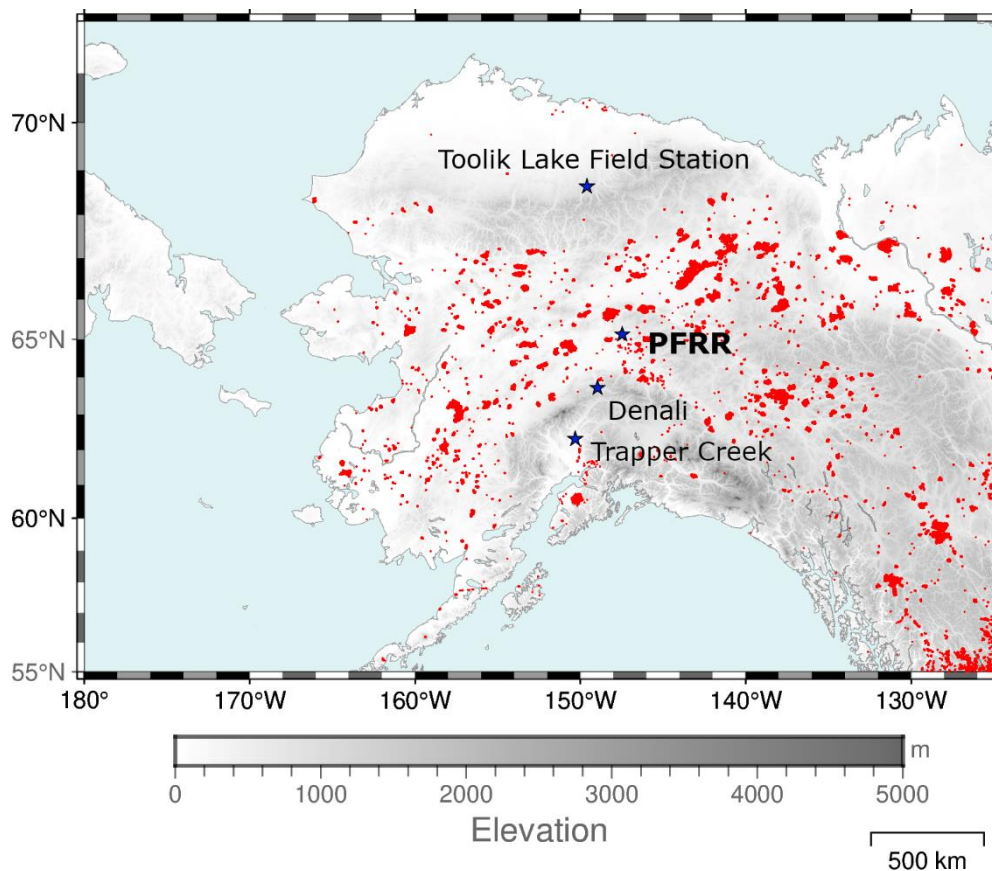
62 BC mass concentrations have long been observed in the atmosphere and snow at Utqiagvik (Barrow) (Eck et al., 2009; Garrett
63 et al., 2011; Mori et al., 2020), which is a high Arctic coastal tundra site. Campaign studies on atmospheric BC mass
64 concentrations were also conducted in interior Alaska using aircrafts (Kondo et al., 2011b; Bian et al., 2013; Creamean et al.,
65 2018). These campaign observations have provided an in-depth understanding of aerosol parameters related to wildfires.
66 However, separate long-term observations of BC mass concentrations are required to characterize annual trends and seasonality.
67 Fewer studies have reported atmospheric BC mass concentrations in interior and coastal Alaska (Polissar et al., 1996, 1998;
68 Eck et al., 2009; Mouteva et al., 2015) and the high Arctic coastal site (Alert, Canada) (Garrett et al., 2011). To understand the
69 long-term variations in BC mass concentration and their impacts on the climate and environment, more BC observation data
70 from interior Alaska are needed (AMAP, 2011). In this study, we aimed to investigate detailed variations in BC mass
71 concentration and its sources, with a focus on forest wildfires in interior Alaska, based on our monitoring of BC and CO at the
72 Poker Flat Research Range (PFRR), which is a University of Alaska Fairbanks (UAF) observational site in interior Alaska.
73

74 **2 Method**

75 **2.1 Observation site**

76 We conducted BC and CO monitoring at the PFRR (65.12° N, 147.43° W, 500 m a.s.l.) starting in April 2016. The PFRR is
77 located in the centre of interior Alaska (Figure 1), approximately 35 km northeast of Fairbanks. The PFRR is surrounded by a
78 predominant evergreen needled-leaved (black spruce; *Picea mariana*) forest with shrubland and herbaceous vegetation
79 (Buchhorn et al., 2020). Note, that the effects of deposition by trees and canopies can be ignored because the laboratory is
80 located on a mountain hill, with non-tall (~2 m) sparse black spruce forest. In this study, BC and CO monitoring results were
81 analysed between April 2016 and December 2020.

82



83

84 Figure 1. A map that shows the location of the PFRR and other sites compared in Section 3.2 (Trapper Creek, Denali, and
 85 Toolik Lake Field Station). All hot spots (larger than 0.3 MW in FRP) observed in the USA and Canada by VIIRS between
 86 2016 and 2020 are shown in red colour.

87

88 2.2 Measurements

89 BC was measured by a Continuous Soot Monitoring System (BCM3130, Kanomax, Japan) with a flow rate of 0.78 L min^{-1} at
 90 standard temperature and pressure (STP; 273 K and 1013 hPa). Sample air was introduced using an approximately 10 m
 91 conductive silicone tube (1/2" i.d.) from a height of 5.5 m above the ground. The measurement technique of BCM3130 is
 92 based on filter-based optical absorption, thus other light-absorbing particles and scattering particles can be a source of
 93 interferences on BC measurement (Bond et al., 1999; Kondo et al., 2009). To minimize interferences from these particles,
 94 coarse mode particles (approximately $>1.0 \mu\text{m}$), such as mineral dust, were removed by a $\text{PM}_{1.0}$ cyclone (URG-2000-30ED,

95 URG, USA) operated with a small flow regulation pump ($\sim 4.5 \text{ L min}^{-1}$ at STP). Note, as most BC particles are smaller than 1
96 μm (Bond et al., 2013), BC loss through the $\text{PM}_{1.0}$ cyclone can be ignored. In addition, to remove nonrefractory particles, such
97 as sulfate and organics, the sample air was heated to approximately $300 \text{ }^\circ\text{C}$ using a heated inlet before it was introduced into
98 the instrument. More details of the instrument are described elsewhere (Miyazaki et al., 2008; Kondo et al., 2009, 2011a). One-
99 minute observation data were averaged to hourly data as the primary data. The limit of detection value (LOD) for hourly BC
100 mass concentration was estimated to be 2 ng m^{-3} , which is the sum of average hourly data and $3\text{-}\sigma$ values using 18 hours of
101 particle-free air measurements.

102 The CO mixing ratio was measured by an infrared absorption photometer (48iTLE, Thermo Fisher Scientific, USA) with a
103 flow rate of 0.5 L min^{-1} . Sample air was introduced using an approximately 10 m PFA tube from a height of 5.5 m above the
104 ground. Internal zero measurements were carried out for 20 minutes every hour, and the CO mixing ratio was estimated from
105 the difference in absorption between the sample and the zero measurements. Span gas (0.99 ppm CO/N_2 , Taiyo-Nissan, Tokyo,
106 Japan) calibration was performed in April 2016. We calculated ΔCO as the enhancement in CO from background levels (14
107 days moving 5-percentile values of observation results). Cases with hourly ΔCO larger than $3\text{-}\sigma$ (13.9 ppb in median, $1\text{-}\sigma$ was
108 derived from zero mode measurements before and after the hourly ambient air observations) were only used for analysis. To
109 validate our CO observations, we compared our observed CO mixing ratio with aircraft observations (less than 500 m AGL
110 above the PFRR) provided by the NOAA Global Monitoring Laboratory (<https://doi.org/10.15138/39HR-9N34>; accessed on
111 2 November 2023) (Figure S1), confirming a good agreement between these two observation results.

112

113 **2.3 Model calculation**

114 The FLEXPART (FLEXible PARTicle dispersion model)-WRF (Weather Research & Forecast) model was used in backward
115 mode to characterize the source areas and sectors for the sampled air masses at the PFRR. FLEXPART-WRF version 3.3
116 (Brioude et al., 2013) and WRF version 4.4 (Skamarock et al., 2019) were employed for this study. The FLEXPART-WRF
117 model was driven by mass-weighted wind fields and perturbation within the PBL calculated by WRF, which covers the
118 Northern Hemisphere with a 45-km horizontal resolution. The ERA5 global reanalysis (Hersbach et al., 2020) was used as the
119 initial and lateral boundary conditions of WRF, and the meteorological field of WRF was also nudged to ERA5 with e-folding
120 times of 3 hours and 12 hours for wind fields and temperature, respectively. Wet deposition is the major removal process for
121 BC, and the deposition process in FLEXPART version 10 (Grythe et al., 2017) was applied to the FLEXPART-WRF model
122 and was used in this study, with values of 10.0, 1.0, 0.9, and 0.1 employed as the collection efficiencies for wet deposition by
123 rain and snow and the activation efficiencies of cloud condensation nuclei (CCN) and ice nuclei (IN) (C_{rain} , C_{snow} , CCN_{eff} , and
124 IN_{eff}), respectively, which estimated by (Grythe et al., 2017) as the best parameters over several Arctic regions, i.e., Barrow,
125 Alert, and Zeppelin. The FLEXPART-WRF calculation was conducted every 6 hours from April 2016 to December 2020. For

126 each simulation, 40000 particles were released at 0.5×0.5 degrees (horizontally) and from 0 to 200 m AGL (vertically) centred
127 at the PFRR. The particles were tracked for 20 days at 6-hour intervals, and most simulated particles reached PFRR within
128 approximately 10 days (Figure 4(c)). The primary output of the FLEXPART-WRF backward calculations was the potential
129 emission sensitivity (PES), which expresses the residence time of particles at a given location and is used to characterize the
130 transport pathways of the sampled air masses. The concentration of BC was estimated by multiplying PES and emissions based
131 on a procedure reported by Sauvage et al. (2017). ECLIPSE (Evaluating the Climate and Air Quality Impacts of Short-Lived
132 Pollutants) version 6b (Klimont et al., 2017) and GFED (Global Fire Emission Database) version 4.1 (Daily) (van der Werf et
133 al., 2014) were used as the anthropogenic and biomass burning emissions, respectively. Note that the Chinese BC emissions
134 from ECLIPSE version 6b with the monthly profile of version 5 are certified with downwind atmospheric BC observations
135 (Kanaya et al., 2020), while other bottom-up inventories might result in a factor of ~ 2 overestimation. The PES fields were
136 calculated with a horizontal resolution of 0.5×0.5 degrees. The contribution of particles within 100 m from the surface was
137 considered for the calculation of PES for anthropogenic emissions. The plume height of the GFAS (Global Fire Assimilation
138 System) (Di Giuseppe et al., 2017) was also used for the estimation of the injection height for biomass burning emissions. The
139 fractional contribution of anthropogenic emissions was considered using eight sectors in the ECLIPSE emission, i.e., ship, gas
140 flaring, waste incineration, transport, industry, energy, domestic, and agriculture, and the anthropogenic and biomass burning
141 emissions were divided into eight regions, i.e., Europe, Central Asia, Russia, East Asia, Canada, Alaska, USA (excluding
142 Alaska), and Others. The mean age of BC was also estimated by the mean lag time between release and observed time weighted
143 by the amount of emission at each time period within the 20-day backward calculations.

144

145 **2.4 Analysis of the effect of forest wildfire on the BC mass concentration at the PFRR**

146 We characterized the observed BC/ Δ CO ratios, which are known to be valuable indicators of emission sources and combustion
147 conditions (Kondo et al., 2011b; Pan et al., 2017; Selimovic et al., 2019), in terms of fire radiative power (FRP), which accounts
148 for forest wildfire intensity. To do this, we compared the BC/ Δ CO ratio in cases of high BC mass concentrations (see section
149 3.4) observed between June and September (406 hours in total) and FRP observed by the Visible Infrared Imaging Radiometer
150 Suite (VIIRS) on the Suomi NPP satellite. Airmasses were traced for 4 days at the most using the Hybrid Single-Particle
151 Lagrangian Integrated Trajectory model (HYSPLIT; (Stein et al., 2015)) with GDAS1 meteorological datasets (3 h archived
152 $1^\circ \times 1^\circ$ Global Data Assimilation System) from the National Centers for Environmental Prediction
153 (<http://ready.arl.noaa.gov/gdas1.php>; accessed on 2 November 2023). The calculation started from 500 m AGL at the PFRR
154 site, and fire spots were searched along with the trajectories.

155 The BC/ Δ CO ratio is also affected by atmospheric processes (Kanaya et al., 2016; Choi et al., 2020), as only BC is lost via
156 wet removal processes. To extract observation results that were not affected by wet removal processes, we used accumulated

157 precipitation along the trajectory (APT) as an indicator of wet removal processes. Previous studies showed that the BC/ Δ CO
158 ratio can be changed when APT is larger than 1 mm (Choi et al., 2020; Kanaya et al., 2016; Kondo et al., 2011b). Therefore,
159 the duration for the accumulation of fire spots was shortened when APT reached 1 mm or when the trajectory reached ground
160 level. Rectangles were defined with $\pm 0.5^\circ$ in the longitudinal direction and $\pm 0.25^\circ$ in the latitudinal direction centring around
161 hourly air mass positions. Then, the FRP and the number of hot spots (points) were accumulated for individual rectangles over
162 the duration of the trajectories. Finally, the total accumulated FRP (\sum FRP) was divided by the detected total points to yield an
163 index describing the conditions of fires affecting the observed airmasses. As hot spot datasets, VIIRS 375 m
164 (VNP14IMG_TML_NRT) archived datasets (countries were “United States” and “Canada”) from the Fire Information for
165 Resource Management System (FIRMS) website (<https://earthdata.nasa.gov/firms>; accessed on 2 November 2023) were used
166 in this study. The selected confidence levels were ‘nominal’ or ‘high’, and the selected type attributed to thermal anomalies
167 was ‘presumed vegetation fire’. In addition, we used FRP values greater than 0.3 MW for each hot spot because hot spots
168 smaller than 0.3 MW included outliers (Figure S2). Only hot spots that were observed within the previous 24 hours were
169 considered. Through this procedure (hereafter, we simply use ‘back trajectory’), forest wildfires in Alaska and western Canada
170 (\sum FRP>0) were detected in 184 cases of hourly BC observation results. Note that we also confirmed that no back trajectories
171 could suggest forest wildfires in other seasons.

172

173 **3 Results and discussion**

174 **3.1 Time series of observed BC and CO concentrations**

175 The time series of BC mass concentration and CO mixing ratio are shown in Figure 2, and those of annual median, 10th, and
176 90th percentile values are summarized in Table 1. The median hourly BC mass concentration and 10th and 90th percentile
177 values throughout the observation period were 13, 3, and 56 ng m⁻³, respectively. No clear increase in annual median BC mass
178 concentration was observed (Table 1). Observed median BC mass concentrations were the same level as previous reports at
179 Utqiagvik (Barrow) (12 ng m⁻³), which showed BC mass concentration over the long term using the same instrument
180 (BCM3130) employed in this study (Sinha et al., 2017; Mori et al., 2020). Abrupt peaks (up to 5540 ng m⁻³) were occasionally
181 observed during summer at PFRR, but these peaks were not observed at Utqiagvik. On the other hand, increases in BC mass
182 concentrations were reported in Utqiagvik between January and March, while not in PFRR. These different variations may be
183 attributed to the topological separation by the Brooks mountain range and to the polar dome structure (Quinn et al., 2007;
184 Sharma et al., 2013).

185 The median, 10th, and 90th percentiles of hourly CO mixing ratios throughout the observation period were 124.7, 99.0, and
186 148.2 ppb, respectively. Similar to BC, increases in the annual median CO mixing ratio were not observed, but contrary to the

187 BC mass concentration, the CO mixing ratio showed clear seasonal variation, high in spring (between February and April,
188 143.5 ppb in the median) and low in summer (July and August, 103.3 ppb in the median) (Figure 2(b)). These observed CO
189 mixing ratios and seasonal variations were consistent with previous studies that reported the CO mixing ratio at the PFRR
190 (Kasai et al., 2005; Yurganov et al., 1998). In summer, CO peaks coincident with BC mass concentration were found,
191 suggesting a common emission source for both BC and CO.

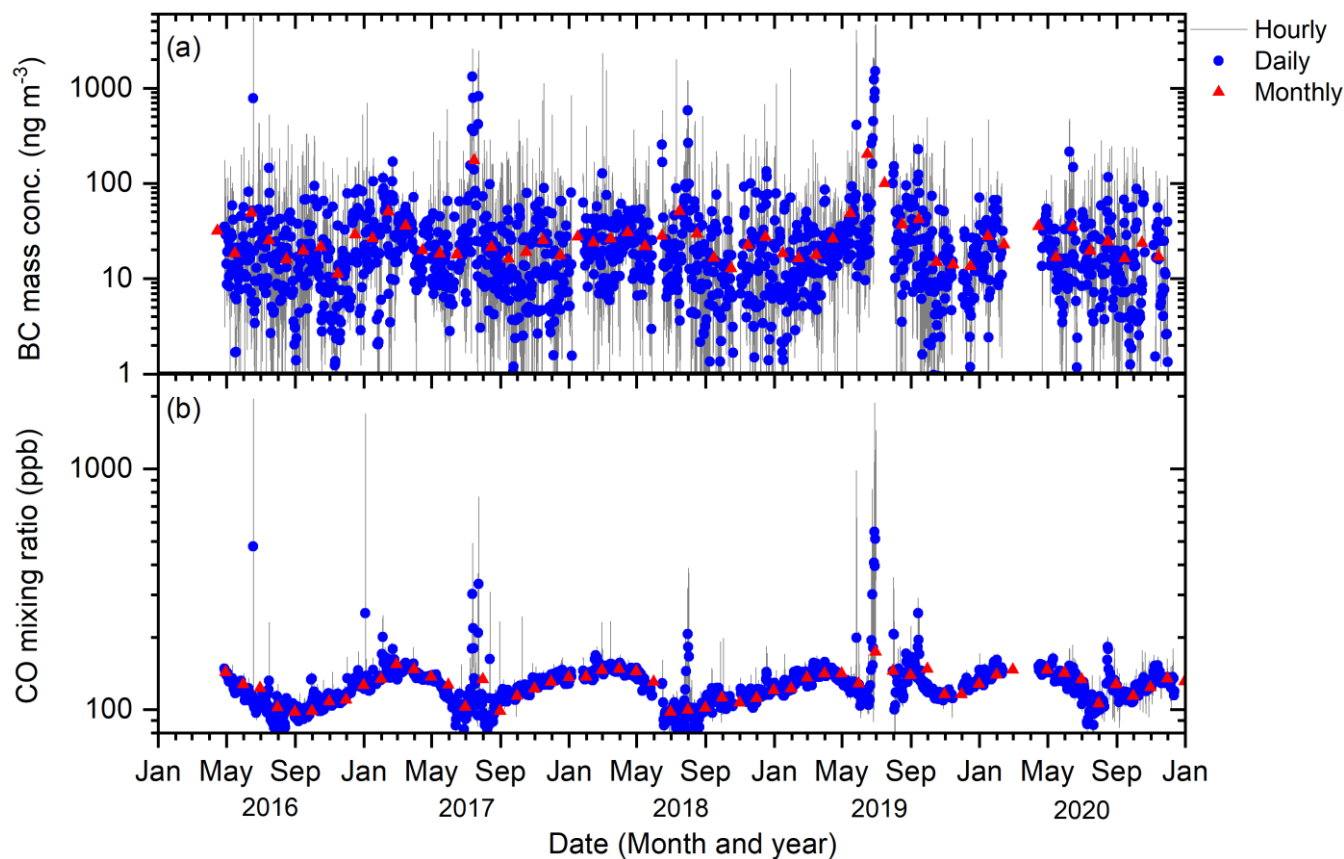
192

193 Table 1. Annual summary of the observed hourly BC mass concentration and CO mixing ratio at the PFRR.

Year	BC (ng m^{-3})			CO (ppb)		
	Median	10th percentile	90th percentile	Median	10th percentile	90th percentile
2016 ^a	11	2	49	109.7	93.1	130.3
2017	15	3	65	128.2	100.5	148.8
2018	14	3	53	118.2	93.3	149.4
2019	15	3	63	128.4	113.1	150.8
2020	13	3	50	131.3	107.5	150.6

194 ^a Observations started on 28 April 2016.

195



196

197 Figure 2. Time series of (a) BC mass concentration and (b) CO mixing ratio observed at the PFRR from April 2016 to
198 December 2020. Grey lines, blue filled circles, and red filled triangles in both (a) and (b) show hourly, daily, and monthly
199 averages, respectively.

200

201 **3.2 Comparisons with other observation sites**

202 We compared the BC observation results from the PFRR to those from other Alaskan sites (Table 2 and Figure S3), i.e.,
203 Trapper Creek (TRCR), Denali (DENA), and Toolik Lake Field Station (TOOL), using datasets for 24-hour filter samples
204 collected every three days. The datasets were from the thermal/optical reflectance method at DENA, TRCR, and TOOL
205 (<http://views.cira.colostate.edu/fed/QueryWizard/>; accessed on 2 November 2023). A systematic bias might be present in terms
206 of the methods used, but it is most likely within a factor of 2 from the actual conditions based on comparisons with recent data
207 at various sites (Miyazaki et al., 2008; Kondo et al., 2009; Kanaya et al., 2008; Kondo et al., 2011a; Ohata et al., 2021; Sinha
208 et al., 2017). For the BC mass concentration observed at TRCR, DENA, and TOOL, datasets flagged V0 (valid value) were
209 selected.

210 The BC mass concentration peaks were nearly coincided for the PFRR, DENA, TRCR, and TOOL (Figure S3). The median
211 and maximum daily BC mass concentrations observed at each site are summarized in Table 2. The median BC mass
212 concentrations at DENA, TRCR, and TOOL were larger than those at the PFRR by 6–19 ng m⁻³ (Table 2), but the significance
213 of the difference is unclear considering methodological differences and associated uncertainties (precision). Here, the
214 uncertainties of the thermal/optical reflectance method varied between 12 and 14 ng m⁻³ in median values during the whole
215 observation period. Note that our BC observation, which had a better LOD (2 ng m⁻³) and higher temporal resolution (1 hour),
216 could provide more reliable data in this low range. On the other hand, the maximum BC mass concentrations were higher at
217 the PFRR within the period with common BC peaks than at TRCR and TOOL but similar at DENA (Table 2). This indicates
218 that strong BC emissions in central Alaska were better captured at the PFRR than at other observation sites because PFRR is
219 the only BC-measuring site located in the central interior of Alaska and is surrounded by forest wildfire occurring regions
220 while other BC observation sites are located on the edge or outside of interior Alaska. We will discuss source and emission
221 ratio characterization in Sections 3.4 and 3.5 by fully utilizing the superior temporal resolution and accuracy of our
222 observations.

223

224

225

226

227

228 Table 2. Summary of the locations of the observation sites and the BC mass concentrations in the interior Alaska.

Site	Latitude (° N)	Longitude (° W)	Altitude (m a.s.l)	Daily BC mass concentration (ng m ⁻³)	
				Median	Maximum
PFRR ^a (this study)	65.12	147.43	500	18	920
TRCR ^{a, b, c}	62.32	150.32	155	37	570
DENA ^{a, b, d}	63.73	148.97	658	24	1044
TOOL ^{b, e, f}	68.64	149.61	740	28	643

229 ^a Period of data used: 28 April 2016 – 2 December 2020.230 ^b Data utilised from the IMPROVE Network.231 ^c TRCR: Trapper Creek.232 ^d DENA: Denali.233 ^e TOOL: Toolik Lake Field Station.234 ^f Period of data used: 13 November 2018 – 2 December 2020.

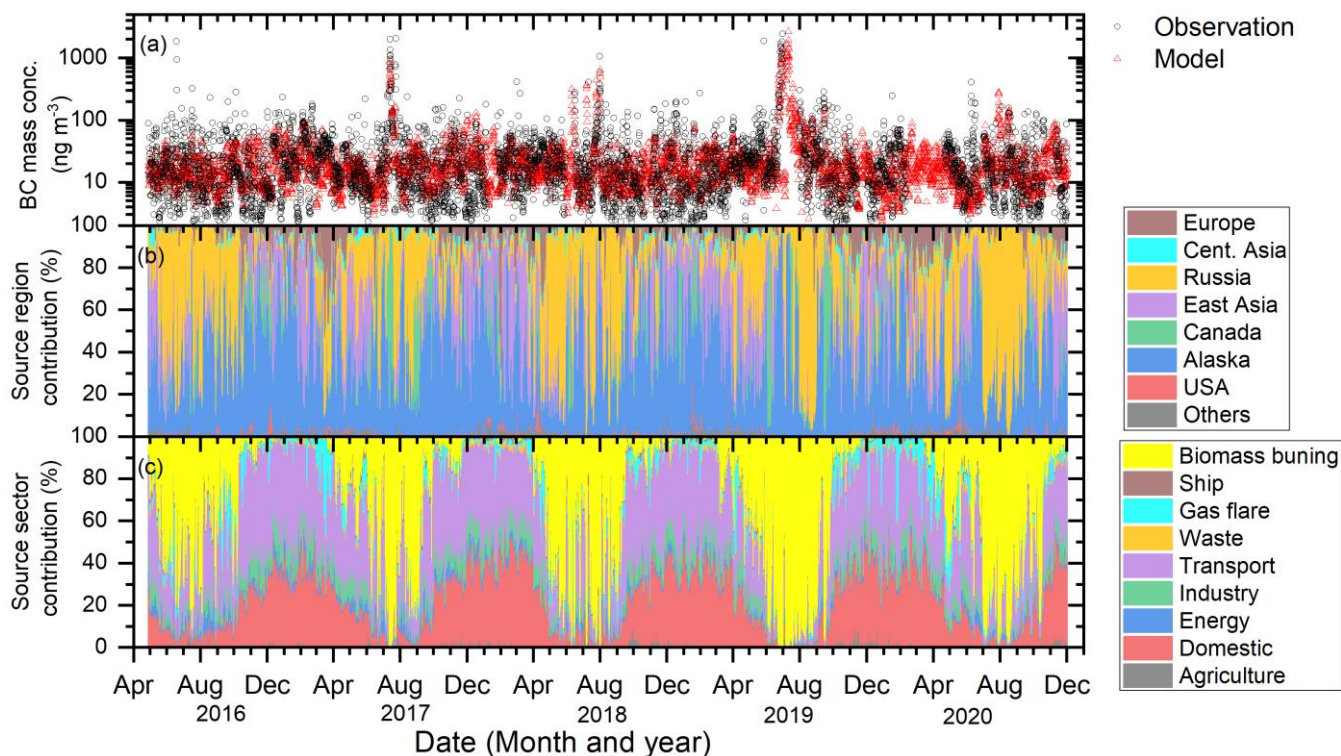
235

236 **3.3 Comparison of observation and model simulations and possible BC sources**

237 Figure 3(a) shows a time series of 6-hour averages of the observation data and 6-hourly BC mass concentrations estimated by
 238 FLEXPART-WRF simulations. FLEXPART-WRF could capture the high BC mass concentration peaks (Figure 3(a)) with a
 239 correlation coefficient of 0.7 (Figure S4). The median of the simulated/observed ratio (observation data > LOD in this case)
 240 was 1.0 for the whole observation period, indicating good agreement between the model simulation and observations.

241 The source region and source sector contributions derived from the FLEXPART-WRF simulation are shown in Figure 3(b)
 242 and (c). The BC source sectors and regions varied clearly according to the season (Figure 3(b) and (c)). In the warm season
 243 (between May and September), the possible BC source regions were Russia (3.6–74 % in the 10–90 percentile) and Alaska
 244 (12–85 % in the 10–90 percentile) and sometimes Canada (1.0–21 % in the 10–90 percentile) (Figure 3(b)), and the possible
 245 source sector was estimated to be biomass burning (8.1–88 % in the 10–90 percentile) (Figure 3(c)), especially when BC mass
 246 concentration was high, suggesting that BC contributions from biomass burning that occurred in Russia, Alaska, and Canada
 247 are dominant for BC mass concentrations at the PFRR. As snow cover disappears from the ground and the atmospheric
 248 conditions become drier, forest wildfires caused by lightning increase in these warm seasons (Reap, 1991; Kaplan and Lau,
 249 2021), resulting in increases in BC emissions from biomass burning (AMAP, 2021). We will focus on these cases of high BC
 250 mass concentrations from Alaska and discuss the relationship between forest wildfire intensity and the BC/ Δ CO ratio in the
 251 following section.

252 On the other hand, in the cold seasons (between October and April), the domestic (24–48 % in the 10–90 percentile) and
 253 transport sectors (25–48 % in the 10–90 percentile) were estimated to be possible dominant BC source sectors (Figure 3(c)).
 254 The dominant source region was Alaska (19–88 % in the 10–90 percentile), and occasionally, Russia (0.89–31 % in the 10–
 255 90 percentile) and East Asia (1.2–41 % in the 10–90 percentile) contributed to the BC mass concentration in PFRR (Figure
 256 3(b)).
 257

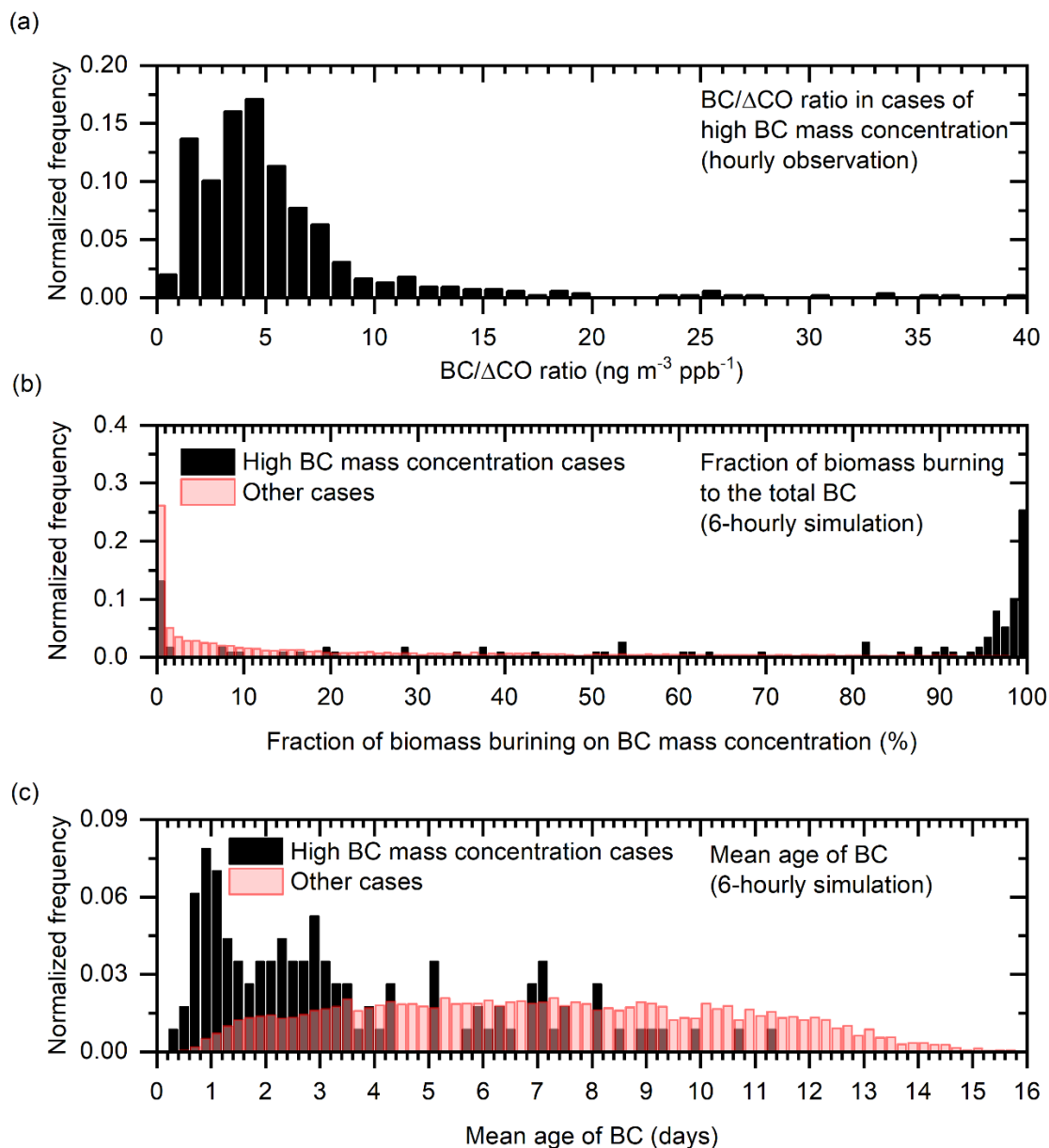


258
 259 Figure 3. Time series of (a) BC mass concentrations, (b) attribution of BC at the PFRR to source regions, and (c) to source
 260 sectors. Black open circles and red open triangles in (a) show the 6-hour average observations and 6-hourly simulations,
 261 respectively. Individual colour bars in (b) and (c) depict the estimated contributions from the source regions and sectors,
 262 respectively. The FLEXPART-WRF model was used for all simulations.

263
 264 **3.4 Biomass burning contribution for cases of high BC mass concentrations**

265 Hereafter, we focus on cases of high BC mass concentrations at the PFRR (647 hours in total), which were selected with the
 266 98 percentile value (171 ng m^{-3}) as the threshold for the hourly BC mass concentration. The cumulative BC mass concentration

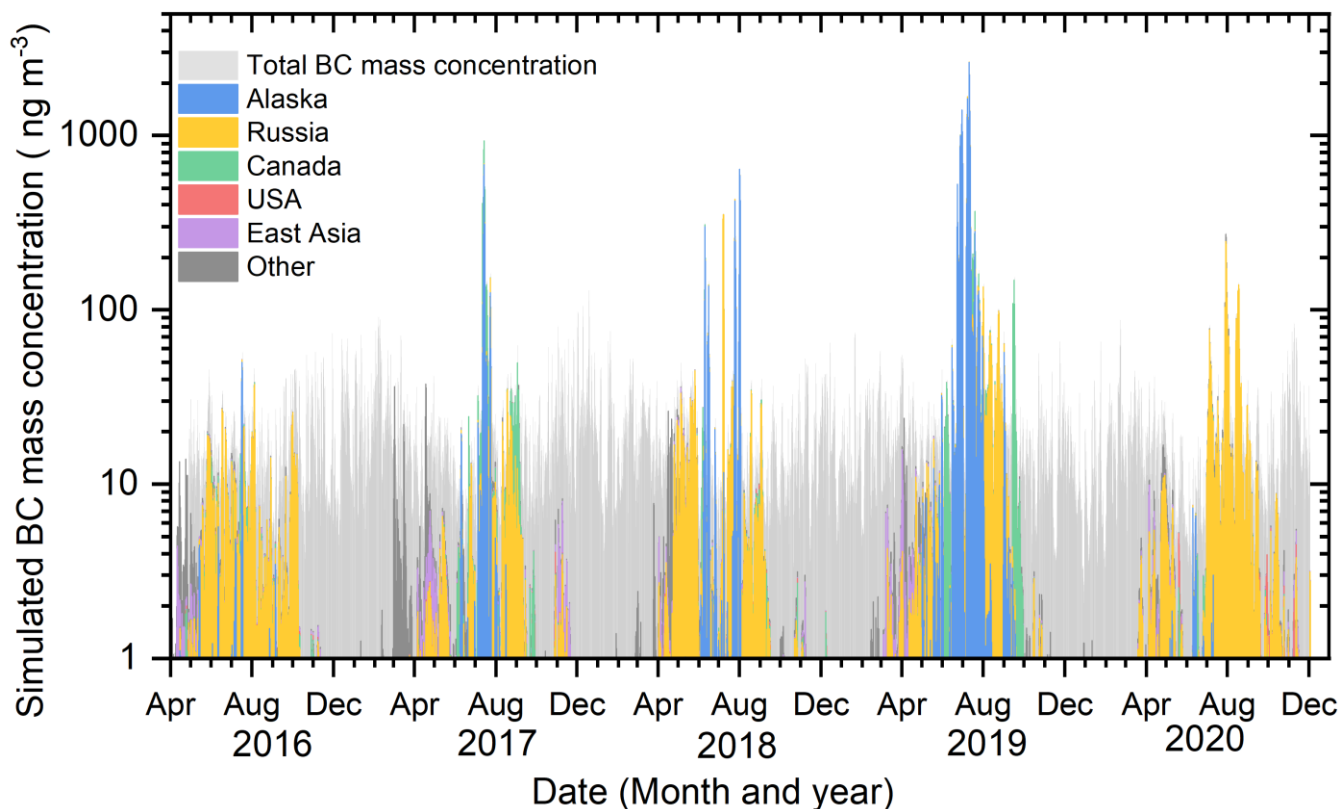
267 observed in these cases of high BC mass concentrations accounted for 5.7–43 % of the annual BC mass concentration, although
268 the duration of these periods was very short (17–187 hours in a year). Most of these cases of high BC mass concentrations
269 (approximately 90 %) were observed in warm seasons (between June and September) and were related to forest wildfires in
270 Alaska. The median CO mixing ratio for the cases of high BC mass concentrations (174.7 ppb) was also higher than that in
271 other periods (124.7 ppb), suggesting that both BC and CO were emitted from forest wildfires (see Section 3.3).
272 The normalized frequency distribution of the BC/ Δ CO ratio for the cases of high BC mass concentrations is shown in Figure
273 4(a). The median, 10th, and 90th percentile values of the BC/ Δ CO ratio during these periods were 4.7, 1.8, and 18 ng m⁻³ ppb⁻¹,
274 respectively. These observed BC/ Δ CO ratios in the cases of high BC mass concentrations were in the same range or
275 sometimes higher than those in previous studies that reported the BC/ Δ CO ratios from boreal forest wildfire emissions in
276 Canada (Kondo et al., 2011b) and Siberia (Paris et al., 2009; Chi et al., 2013; Vasileva et al., 2017).
277 The medians of the fractional contributions of biomass burning on total BC mass concentrations and the mean age of BC
278 estimated by the FLEXPART-WRF simulation in these cases of high BC mass concentrations (>154 ng m⁻³ in 6-hourly
279 average) were higher and shorter (95.5 % and 2.6 days) than those in other periods (7.6 % and 6.9 days) (Figure 4(b) and (c)),
280 indicating a strong contribution of BC from neighbouring forest wildfires (Figure S5). We also calculated the 6-hourly mass-
281 weighted biomass burning contributions from individual source regions (6 categories based on Figure 3(b), Central Asia and
282 Europe are included in Others) to the BC mass concentrations at the PFRR (Figure 5). As a result, we found that large peaks,
283 such as those observed between June and August in 2017, 2018, and 2019, coincided well with the peaks of BC contributions
284 mostly from forest wildfires in Alaska (Figure S5). BC from forest wildfires that occurred in western Canada also affected the
285 BC concentration at PFRR (Figure S6) but to a lesser frequency. Russia was also estimated as an effective BC source region
286 (Figure 3), but BC concentration did not exceed 0.1 μ g m⁻³ in most cases (Figure 5). These results confirmed that the observed
287 cases of high BC mass concentrations were primarily affected by local forest wildfires in Alaska. These peaks were widely
288 observed in Alaska (Section 3.2) and imply a large impact of local forest wildfires on BC mass concentration in this region.
289 However, when these cases of high BC mass concentrations were selected, the median of the simulated/observed ratio was
290 0.30, indicating underestimation in the model simulation (possibly due to insufficient spatial resolution for neighbouring forest
291 wildfires and difficulties in representing the vertical profiles of BC emissions) or/and in emission inventories in the cases of
292 high BC mass concentrations. Several studies have indicated that differences in different inventories cause large uncertainties
293 in model estimates of BC emissions, atmospheric concentrations, and radiative impacts, especially in boreal North America
294 (Carter et al., 2020; Pan et al., 2020). The impact of different inventories on model estimates will be discussed in the future.
295
296



297

298 Figure 4. (a) Histogram of the observed hourly BC/ΔCO ratio at the PFRR in cases of high BC mass concentrations (>98
 299 percentile). Histograms of the simulated 6-hourly (b) fractions of BC mass concentrations from biomass burning to the total
 300 BC and (c) mean age of BC estimated by the FLEXPART-WRF model. Black and red bars in (b) and (c) show the cases of
 301 high BC mass concentrations and the other cases (<98 percentile), respectively.

302



304

305 Figure 5. A time series of the 6-hourly BC mass concentrations at the PFRR simulated by the FLEXPART-WRF model. Light
 306 grey bars show the total BC mass concentrations. Other individual colour bars (overlaid on the light grey bars) show the BC
 307 mass concentrations for biomass burning from each source region.

308

309

310 3.5 Relationship between the BC/ Δ CO ratio and FRP

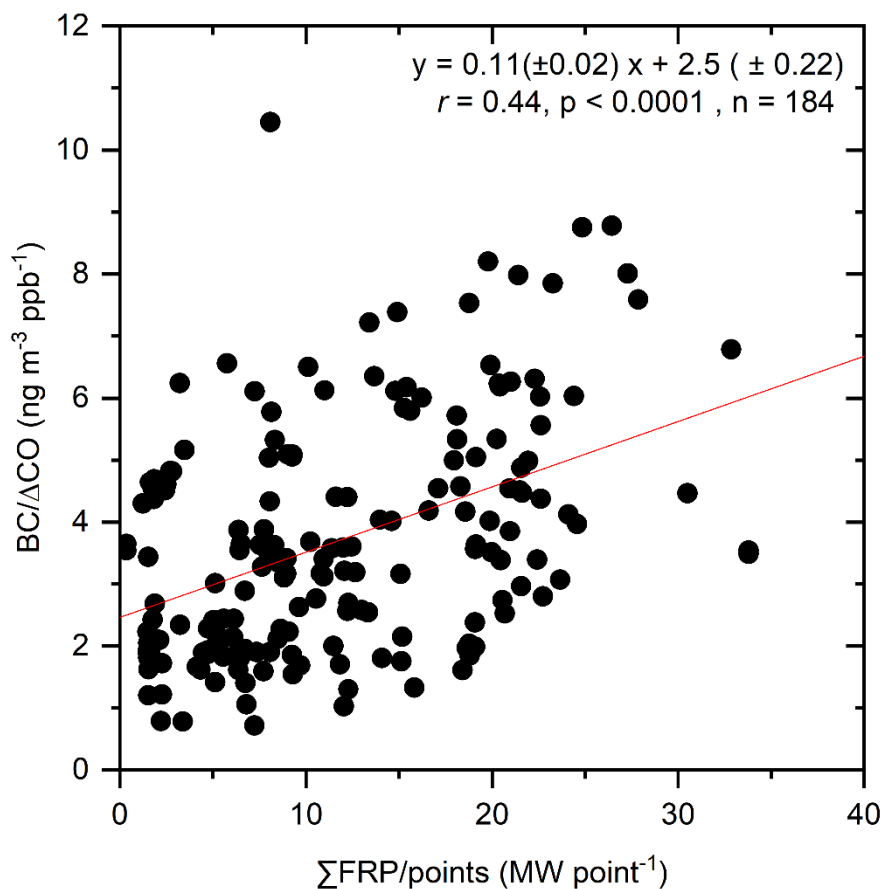
311 In the previous section, we showed that most cases of high BC mass concentrations were related to forest wildfires in Alaska.
 312 Increases in biomass-burning-derived BC/ Δ CO ratios with combustion efficiency were suggested from an observational study
 313 on boreal forest wildfire (Kondo et al., 2011b) and from laboratory-scale burning experiments of crop residues (Pan et al.,
 314 2017); however, in-depth studies examining variabilities in BC/ Δ CO ratios based on long-term, near-forest observations have
 315 not been conducted. To consider the possibility that combustion conditions (flaming and smouldering) primarily control the

316 BC/ Δ CO ratio, we are going to investigate the relationship between the BC/ Δ CO ratio and forest wildfire intensity in this
317 section.

318 We found a positive correlation ($r = 0.44$, $p < 0.0001$, $n = 184$) between the BC/ Δ CO ratio and Σ FRP/point values (Figure 6).
319 This positive correlation between the BC/ Δ CO ratio and Σ FRP/point values, represented for the first time to our knowledge,
320 is qualitatively consistent with previous studies that showed that high combustion efficiency (larger than 0.9 in modified
321 combustion efficiency value (MCE)) increased BC/ Δ CO ratios (Selimovic et al., 2019; Kondo et al., 2011b; Pan et al., 2017),
322 which is related to the fact that the BC production process is mostly related to the flaming process (high MCE), while that of
323 CO is related to the smouldering process (low MCE). For example, Pan et al. (2017) measured BC, CO, and CO₂ from biomass
324 burning in small-scale combustion experiments. In their experiment, dry and wet wheat straw samples and dry rapeseed plant
325 samples were burned, and the time evolution of BC/ Δ CO ratio and MCE were observed. They reported that BC is mostly
326 produced during the flaming process, and the evolution of the BC/ Δ CO ratio which depends on the combustion stage could be
327 confirmed ($13.9 \pm 10.1 \text{ ng m}^{-3} \text{ ppbv}^{-1}$ for MCE larger than 0.95 cases, and less than $7.1 \text{ ng m}^{-3} \text{ ppbv}^{-1}$ for MCE smaller than
328 0.96 cases). Although these BC/ Δ CO ratios are larger than our observed BC/ Δ CO ratio, differences in fuels might be a possible
329 reason. Selimovic et al. (2018) also burned some types of fuels, including coniferous trees, in a large indoor combustion facility
330 and measured BC, CO, and CO₂ with various other chemical species. They reported a high BC/ Δ CO ratio ($13.8 \text{ ng m}^{-3} \text{ ppbv}^{-1}$
331 on average) and a low BC/ Δ CO ratio ($4.7 \text{ ng m}^{-3} \text{ ppbv}^{-1}$ on average) in the condition of flaming-dominated and smouldering-
332 dominated, respectively, in the same range as our observed values. Moreover, Chakrabarty et al. (2016) tested Alaskan peat
333 and Siberian peat in the combustion chamber under smouldering conditions, and low BC/ Δ CO ratios ($1.2\text{--}2.6 \text{ ng m}^{-3} \text{ ppbv}^{-1}$)
334 were reported. The positive relationship between the BC/ Δ CO ratio and MCE is also observed in the field measurements
335 (Kondo et al., 2011b; Selimovic et al., 2019). Although MCE and FRP are different parameters, both parameters indicate
336 combustion conditions and have a strong correlation (Wiggins et al., 2020). Therefore, for the first time, we report a positive
337 correlation between the BC/ Δ CO ratio and FRP as a combustion condition indicator. The wide range of BC/ Δ CO ratios reported
338 from boreal forest wildfires, from $1.7\text{--}3.4 \text{ ng m}^{-3} \text{ ppbv}^{-1}$ (Kondo et al., 2011b) to $6.1\text{--}6.3 \text{ ng m}^{-3} \text{ ppbv}^{-1}$ (Vasileva et al., 2017),
339 could be better explained when the index introduced here (Σ FRP/point) is considered. This relationship should be taken into
340 account when constructing future emission inventories from boreal forest wildfires.

341 A positive correlation was found after optimizing the spatial window size ($\pm 0.5^\circ$ in the longitudinal direction and $\pm 0.25^\circ$ in
342 the latitudinal direction), in which hot spots were taken into account for each hour along the trajectory (from -96 to 0 hours),
343 and the associated time window was used to determine coincident fires that affected the observations (from -24 to 0 hours).
344 Based on the spatial resolution of GDAS1 ($1^\circ \times 1^\circ$), we set our initial windows as $\pm 0.5^\circ$ for latitude and longitude. However,
345 PFRR is in a high latitude and the geometrical length of latitude is approximately 2 times longer than that of longitude. For
346 this reason, we defined latitudinal width as $\pm 0.25^\circ$ finally. Although we tested finer window size cases, a similar positive trend

347 was confirmed. The remaining scatter might have arisen from differences in the detection of hot spots in the presence of clouds
348 (Li et al., 2018). To overcome shortcomings in hot spot detection, improvements in the frequency of hot spot scanning should
349 be made, for example, via the use of MODerate Resolution Imaging Spectroradiometer (MODIS) combined with VIIRS
350 observations; it should be noted, however, that there is a bias in FRP observations between MODIS and VIIRS, especially for
351 boreal forests (Li et al., 2018). Improvements in the accuracy and consistency of FRP analysis between multiple satellite
352 observations can facilitate a more in-depth understanding of the relationship between FRP and the BC/ Δ CO ratio.
353 The simulated/observed ratios in cases of high BC mass concentrations were low (0.30, Section 3.3), contrary to the good
354 agreement observed in overall cases (1.0, Section 3.3). The BC/ Δ CO ratios in commonly used emission inventories are 4.9 ng
355 m⁻³ ppb⁻¹ for GFED4s (van der Werf et al., 2017) and 4.4 ng m⁻³ ppb⁻¹ for Andreae (2019) and are in a range similar to that of
356 our median BC/ Δ CO ratio. However, our observed BC/ Δ CO ratios in cases of high BC mass concentrations for forest wildfires
357 had a broad range between 1.7 and 7.3 ng m⁻³ ppb⁻¹ at the 10 and 90 percentiles (median was 4.2 ng m⁻³ ppb⁻¹), respectively,
358 related to the Σ FRP/point values. This implies that the BC emission factors from biomass burning could vary depending on
359 the FRP. Although several previous inventory studies used FRP for the estimation of activity data (Carter et al., 2020), namely,
360 fuel burned or burned area, no inventories included the evolution of the emission factors of BC and/or CO. Our findings suggest
361 the potential for improving BC emission inventories and/or emission factors by using FRP. In addition, BC emission estimation
362 using satellites would be improved by using our results. CO emissions estimated by satellite observations are sometimes used
363 to estimate other pollutant emissions from forest fires using emission ratios derived from in situ measurements (Zheng et al.,
364 2023). As its extension, BC emissions could be estimated, regarding our quantified BC/ Δ CO ratios and their evolutions with
365 FRP directly as the emission ratio of BC to CO. The frequency of boreal forest fires may increase in the future (Box et al.,
366 2019; Hu et al., 2015); as a result, their impact on climate and air quality might become more severe in Alaska and the Arctic
367 (Kim et al., 2005; Schmale et al., 2018; Stohl et al., 2006). Our long-term observations of BC and CO at an hourly temporal
368 resolution in the interior of Alaska provide unique information to test model simulations and emission inventories relevant to
369 the climate and air quality of the Arctic.
370



371

372 Figure 6. The scatter plot (black filled circles) between the hourly BC/ΔCO ratio observed at the PFRR and the Σ FRP/point
 373 values in cases of high BC concentrations (>98 percentile). Data from June to September were analyzed. The Σ FRP/point
 374 values are the average FRP of the hot spots (points) present along the backward trajectories from the PFRR (see section 2.4).
 375 A red line indicates the result of a linear regression fit.

376 4 Conclusion

377 We showed key features of the BC and CO concentrations observed at the PFRR in interior Alaska since 2016 in this paper.
 378 The annual medians of the BC mass concentration and CO mixing ratio were 11–15 ng m⁻³ and 109.7–131.3 ppb, respectively.
 379 Large and short-term increases in BC mass concentrations were sometimes observed between June and September. A clear
 380 seasonal variation was observed in the CO mixing ratio, which was high in spring (between February and April, 143.5 ppb in
 381 the median) and low in summer (July and August, 103.3 ppb in the median). The CO mixing ratio coincided with the high BC
 382 mass concentration peaks, suggesting a strong contribution from forest wildfires to BC and CO concentrations.

383 The BC mass concentrations observed at other sites in Alaska, i.e., DENA, TRCR, and TOOL, were compared with our results.
384 The annual median BC mass concentrations at the PFRR were lower than those at TRCR, DENA, and TOOL, but coinciding
385 BC mass concentration peaks were found at these observation sites. In these cases of high BC mass concentrations, BC mass
386 concentrations at the PFRR were larger than those at TRCR and TOOL but similar at DENA, indicating that strong BC
387 emissions from forest wildfires occurred in interior Alaska and affected broad areas in Alaska.
388 The dominance of forest wildfires in Alaska as a major cause of high BC mass concentration was also supported by the model
389 simulations. We simulated BC mass concentration using the FLEXPART-WRF model and compared the simulations with the
390 observation results. The model simulation could capture observational results ($r = 0.70$) in which the median
391 simulated/observed ratio was 1.0. The estimated BC source sectors and regions were biomass burning from Russia, Alaska,
392 and sometimes Canada between May and September, while those for other periods were domestic sources and transport and
393 were mainly from Alaska.
394 When we focused on cases of high BC mass concentrations (greater than 98 percentile values), we found that forest wildfires
395 occurring in Alaska were the dominant source of BC in those cases from the model simulation results. The mean ages of BC
396 and biomass burning contributions in these cases of high BC mass concentrations estimated by FLEXPART-WRF were 2.6
397 days and 95.5 %, respectively, relatively shorter and higher than those in other cases (6.9 days and 7.6 %, respectively). The
398 peaks of the calculated biomass burning contributions from Alaska to BC mass concentrations at the PFRR coincided well
399 with observed and simulated peaks in cases of high BC mass concentrations, suggesting that the forest wildfires that occurred
400 around the PFRR are important.
401 The median observed BC/ Δ CO ratio in cases of high BC mass concentrations related to forest wildfires was $4.2 \text{ ng m}^{-3} \text{ ppb}^{-1}$
402 and was in the same range as that in previous studies reporting the BC/ Δ CO ratio of boreal forest wildfire emissions. Finally,
403 we tracked air mass origin for 4 days using the HYSPLIT model with FRP satellite observations in these cases and investigated
404 the relationship between the observed BC/ Δ CO ratio and FRP, which was normalized by the number of hot spots (points)
405 observed by VIIRS. A positive correlation was found between these parameters ($r = 0.44$). For the first time, the properties of
406 the BC/ Δ CO ratio from boreal forest wildfires were systematically characterized in terms of FRP, suggesting the potential to
407 improve emission inventories and/or emission factors by using FRP.
408

409 **Data availability**

410 The BC and CO observation results are available online (<https://ads.nipr.ac.jp/dataset/A20241101-003>). We used public data
411 for BC observation results at Denali, Trapper Creek, and Toolik Lake Field Station
412 (<http://views.cira.colostate.edu/fed/QueryWizard/>).
413

414 **Supplement**

415 The supplement related to this article is available online at <https://doi.org/xxxxxxx>.

416

417 **Author contributions**

418 TK, FT, CZ, YKi, and YKa conducted and recorded observations for BC and CO at the PFRR site. MT conducted the
419 FLEXPART-WRF model simulations. YKi assisted in the fieldwork at the PFRR site. TK, FT, MP, and YKa summarized the
420 observation results, and TK wrote the first draft with MT. All authors contributed to the discussion and writing of the
421 manuscript.

422

423 **Competing interests**

424 At least one of the (co-)authors is a member of the editorial board of Atmospheric Chemistry and Physics.

425

426 **Acknowledgement**

427 The authors acknowledge technical support from Dr. Takuma Miyakawa, a researcher at JAMSTEC and help with field work
428 from Dr. Hideki Kobayashi, a researcher at JAMSTEC. The authors also thank all the supporting members at JAMSTEC. The
429 authors thank NOAA ARL for providing the CO aircraft observation data, HYSPLIT model, and GDAS1 meteorological data.
430 We also thank the IMPROVE network. IMPROVE is a collaborative association of state, tribal, and federal agencies and
431 international partners. The US Environmental Protection Agency is the primary funding source, with contracting and research
432 support from the National Park Service. The Air Quality Group at the University of California, Davis, was the central analytical
433 laboratory, and carbon analysis was carried out by the Desert Research Institute. We also thank the anonymous reviewers for
434 their precise and valuable comments that greatly improved the paper.

435

436 **Financial support**

437 This work was funded by the Arctic Challenge for Sustainability II (ArCS II), Program Grant Number JPMXD1420318865,
438 the Arctic Challenge for Sustainability (ArCS), Program Grant Number JPMXD1300000000, and a National Research
439 Foundation of Korea Grant from the Korean Government (MSIT; the Ministry of Science and ICT, NRF-
440 2021M1A5A1065425) (KOPRI-PN24011).

441

442 References

- 443 Aizawa, T., Ishii, M., Oshima, N., Yukimoto, S., and Hasumi, H.: Arctic warming and associated sea ice reduction in the early
444 20th century induced by natural forcings in MRI-ESM2.0 climate simulations and multimodel analyses, *Geophys. Res. Lett.*,
445 48, <https://doi.org/10.1029/2020gl092336>, 2021.
- 446 AMAP: The Impact of Black Carbon on Arctic Climate, Arctic Monitoring and Assessment Programme (AMAP), 2011.
- 447 AMAP: AMAP Assessment 2021: Impacts of Short-lived Climate Forcers on Arctic Climate, Air Quality, and Human Health,
448 Arctic Monitoring and Assessment Programme (AMAP), 2021.
- 449 Aoki, T., Kuchiki, K., Niwano, M., Kodama, Y., Hosaka, M., and Tanaka, T.: Physically based snow albedo model for
450 calculating broadband albedos and the solar heating profile in snowpack for general circulation models, *J. Geophys. Res.*, 116,
451 <https://doi.org/10.1029/2010jd015507>, 2011.
- 452 Bian, H., Colarco, P. R., Chin, M., Chen, G., Rodriguez, J. M., Liang, Q., Blake, D., Chu, D. A., Silva, A. da, Darmenov, A.
453 S., and Others: Source attributions of pollution to the Western Arctic during the NASA ARCTAS field campaign, *Atmos.*
454 *Chem. Phys.*, 13, 4707–4721, <https://doi.org/10.5194/acp-17-15271-2017>, 2013.
- 455 Bond, T. C., Anderson, T. L., and Campbell, D.: Calibration and Intercomparison of Filter-Based Measurements of Visible
456 Light Absorption by Aerosols, *Aerosol Sci. Technol.*, 30, 582–600, <https://doi.org/10.1080/027868299304435>, 1999.
- 457 Bond, T. C., Doherty, S. J., Fahey, D. W., Forster, P. M., Berntsen, T., DeAngelo, B. J., Flanner, M. G., Ghan, S., Kärcher, B.,
458 Koch, D., Kinne, S., Kondo, Y., Quinn, P. K., Sarofim, M. C., Schultz, M. G., Schulz, M., Venkataraman, C., Zhang, H.,
459 Zhang, S., Bellouin, N., Guttikunda, S. K., Hopke, P. K., Jacobson, M. Z., Kaiser, J. W., Klimont, Z., Lohmann, U., Schwarz,
460 J. P., Shindell, D., Storelvmo, T., Warren, S. G., and Zender, C. S.: Bounding the role of black carbon in the climate system:
461 A scientific assessment, *J. Geophys. Res.*, 118, 5380–5552, <https://doi.org/10.1002/jgrd.50171>, 2013.
- 462 Bonfils, C. J. W., Santer, B. D., Fyfe, J. C., Marvel, K., Phillips, T. J., and Zimmerman, S. R. H.: Human influence on joint
463 changes in temperature, rainfall and continental aridity, *Nat. Clim. Chang.*, 10, 726–731, [https://doi.org/10.1038/s41558-020-](https://doi.org/10.1038/s41558-020-020-464)
464 0821-1, 2020.
- 465 Box, J. E., Colgan, W. T., Christensen, T. R., Schmidt, N. M., Lund, M., Parmentier, F.-J. W., Brown, R., Bhatt, U. S.,
466 Euskirchen, E. S., Romanovsky, V. E., and Others: Key indicators of Arctic climate change: 1971–2017, *Environ. Res. Lett.*,
467 14, 045010, <https://doi.org/10.1088/1748-9326/aafc1b>, 2019.
- 468 Bozem, H., Hoor, P., Kunkel, D., Köllner, F., Schneider, J., Herber, A., Schulz, H., Leaitch, W. R., Aliabadi, A. A., Willis, M.
469 D., Burkart, J., and Abbatt, J. P. D.: Characterization of transport regimes and the polar dome during Arctic spring and summer
470 using in situ aircraft measurements, *Atmos. Chem. Phys.*, 19, 15049–15071, <https://doi.org/10.5194/acp-19-15049-2019>, 2019.
- 471 Brioude, J., Arnold, D., Stohl, A., Cassiani, M., Morton, D., Seibert, P., Angevine, W., Evan, S., Dingwell, A., Fast, J. D.,
472 Easter, R. C., Pisso, I., Burkhart, J., and Wotawa, G.: The Lagrangian particle dispersion model FLEXPART-WRF version
473 3.1, *Geoscientific Model Development*, 6, 1889–1904, <https://doi.org/10.5194/gmd-6-1889-2013>, 2013.
- 474 Buchhorn, M., Smets, B., Bertels, L., De Roo, B., Lesiv, M., Tsendbazar, N.-E., Herold, M., and Fritz, S.: Copernicus Global
475 Land Service: Land Cover 100m: collection 3: epoch 2019: Globe, <https://doi.org/10.5281/zenodo.3939050>, 2020.
- 476 Cai, Z., You, Q., Wu, F., Chen, H. W., Chen, D., and Cohen, J.: Arctic Warming Revealed by Multiple CMIP6 Models:
477 Evaluation of Historical Simulations and Quantification of Future Projection Uncertainties, *J. Clim.*, 34, 4871–4892,
478 <https://doi.org/10.1175/JCLI-D-20-0791.1>, 2021.

- 479 Carter, T. S., Heald, C. L., Jimenez, J. L., Campuzano-Jost, P., Kondo, Y., Moteki, N., Schwarz, J. P., Wiedinmyer, C.,
480 Darmenov, A. S., da Silva, A. M., and Kaiser, J. W.: How emissions uncertainty influences the distribution and radiative
481 impacts of smoke from fires in North America, *Atmos. Chem. Phys.*, 20, 2073–2097, [https://doi.org/10.5194/acp-20-2073-](https://doi.org/10.5194/acp-20-2073-482)
482 2020, 2020.
- 483 Chakrabarty, R. K., Gyawali, M., Yatavelli, R. L. N., Pandey, A., Watts, A. C., Knue, J., Chen, L.-W. A., Pattison, R. R.,
484 Tsiabart, A., Samburova, V., and Moosmüller, H.: Brown carbon aerosols from burning of boreal peatlands: microphysical
485 properties, emission factors, and implications for direct radiative forcing, *Atmos. Chem. Phys.*, 16, 3033–3040,
486 <https://doi.org/10.5194/acp-16-3033-2016>, 2016.
- 487 Chi, X., Winderlich, J., Mayer, J.-C., Panov, A. V., Heimann, M., Birmili, W., Heintzenberg, J., Cheng, Y., and Andreae, M.
488 O.: Long-term measurements of aerosol and carbon monoxide at the ZOTTO tall tower to characterize polluted and pristine
489 air in the Siberian taiga, *Atmos. Chem. Phys.*, 13, 12271–12298, <https://doi.org/10.5194/acp-13-12271-2013>, 2013.
- 490 Choi, Y., Kanaya, Y., Takigawa, M., Zhu, C., Park, S.-M., Matsuki, A., Sadanaga, Y., Kim, S.-W., Pan, X., and Pisso, I.:
491 Investigation of the wet removal rate of black carbon in East Asia: Validation of a below-and in-cloud wet removal scheme in
492 FLEXible PARTicle (FLEXPART) model v10. 4, *Atmos. Chem. Phys.*, 20, 13655–13670, [https://doi.org/10.5194/acp-20-](https://doi.org/10.5194/acp-20-493)
493 13655-2020, 2020.
- 494 Cohen, J., Screen, J. A., Furtado, J. C., Barlow, M., Whittleston, D., Coumou, D., Francis, J., Dethloff, K., Entekhabi, D.,
495 Overland, J., and Jones, J.: Recent Arctic amplification and extreme mid-latitude weather, *Nat. Geosci.*, 7, 627–637,
496 <https://doi.org/10.1038/ngeo2234>, 2014.
- 497 Creamean, Maahn, and Boer: The influence of local oil exploration and regional wildfires on summer 2015 aerosol over the
498 North Slope of Alaska, *Atmos. Chem. Phys.*, <https://doi.org/10.5194/acp-18-555-2018>, 2018.
- 499 Di Giuseppe, F., Rémy, S., Pappenberger, F., and Wetterhall, F.: Combining fire radiative power observations with the fire
500 weather index improves the estimation of fire emissions, *Atmos. Chem. Phys. Discuss.*, <https://doi.org/10.5194/acp-2017-790>,
501 2017.
- 502 Duck, T. J., Firanski, B. J., Millet, D. B., Goldstein, A. H., Allan, J., Holzinger, R., Worsnop, D. R., White, A. B., Stohl, A.,
503 Dickinson, C. S., and van Donkelaar, A.: Transport of forest fire emissions from Alaska and the Yukon Territory to Nova
504 Scotia during summer 2004, *J. Geophys. Res.*, 112, <https://doi.org/10.1029/2006jd007716>, 2007.
- 505 Eck, T. F., Holben, B. N., Reid, J. S., Sinyuk, A., Hyer, E. J., O'Neill, N. T., Shaw, G. E., Vande Castle, J. R., Chapin, F. S.,
506 Dubovik, O., Smirnov, A., Vermote, E., Schafer, J. S., Giles, D., Slutsker, I., Sorokine, M., and Newcomb, W. W.: Optical
507 properties of boreal region biomass burning aerosols in central Alaska and seasonal variation of aerosol optical depth at an
508 Arctic coastal site, *J. Geophys. Res.*, 114, <https://doi.org/10.1029/2008jd010870>, 2009.
- 509 Forster, C., Wandering, U., Wotawa, G., James, P., Mattis, I., Althausen, D., Simmonds, P., O'Doherty, S., Jennings, S. G.,
510 Kleefeld, C., Schneider, J., Trickl, T., Kreipl, S., Jäger, H., and Stohl, A.: Transport of boreal forest fire emissions from Canada
511 to Europe, *J. Geophys. Res.*, 106, 22887–22906, <https://doi.org/10.1029/2001jd900115>, 2001.
- 512 Garrett, T. J., Brattström, S., and Sharma, S.: The role of scavenging in the seasonal transport of black carbon and sulfate to
513 the Arctic, *Geophys. Res. Lett.*, <https://doi.org/10.1029/2011GL048221>, 2011.
- 514 Gliß, J., Mortier, A., Schulz, M., Andrews, E., Balkanski, Y., Bauer, S. E., Benedictow, A. M. K., Bian, H., Checa-Garcia, R.,
515 Chin, M., and Others: AeroCom phase III multi-model evaluation of the aerosol life cycle and optical properties using ground-

516 and space-based remote sensing as well as surface in situ observations, *Atmos. Chem. Phys.*, 21, 87–128,
517 <https://doi.org/10.5194/acp-21-87-2021>, 2021.

518 Grythe, H., Kristiansen, N. I., Groot Zwaftink, C. D., Eckhardt, S., Ström, J., Tunved, P., Krejci, R., and Stohl, A.: A new
519 aerosol wet removal scheme for the Lagrangian particle model FLEXPART v10, *Geoscientific Model Development*, 10, 1447–
520 1466, <https://doi.org/10.5194/gmd-10-1447-2017>, 2017.

521 Halofsky, J. E., Peterson, D. L., and Harvey, B. J.: Changing wildfire, changing forests: the effects of climate change on fire
522 regimes and vegetation in the Pacific Northwest, USA, *Fire Ecology*, 16, 4, <https://doi.org/10.1186/s42408-019-0062-8>, 2020.

523 Hersbach, H., Bell, B., Berrisford, P., Hirahara, S., Horányi, A., Muñoz-Sabater, J., Nicolas, J., Peubey, C., Radu, R., Schepers,
524 D., Simmons, A., Soci, C., Abdalla, S., Abellan, X., Balsamo, G., Bechtold, P., Biavati, G., Bidlot, J., Bonavita, M., Chiara,
525 G., Dahlgren, P., Dee, D., Diamantakis, M., Dragani, R., Flemming, J., Forbes, R., Fuentes, M., Geer, A., Haimberger, L.,
526 Healy, S., Hogan, R. J., Hólm, E., Janisková, M., Keeley, S., Laloyaux, P., Lopez, P., Lupu, C., Radnoti, G., Rosnay, P.,
527 Rozum, I., Vamborg, F., Villaume, S., and Jean-Noël Thépaut: The ERA5 global reanalysis, *Quart. J. Roy. Meteor. Soc.*, 146,
528 1999–2049, <https://doi.org/10.1002/qj.3803>, 2020.

529 Hu, F. S., Higuera, P. E., Duffy, P., Chipman, M. L., Rocha, A. V., Young, A. M., Kelly, R., and Dietze, M. C.: Arctic tundra
530 fires: natural variability and responses to climate change, *Front. Ecol. Environ.*, 13, 369–377, <https://doi.org/10.1890/150063>,
531 2015.

532 Ikeda, K., Tanimoto, H., Sugita, T., Akiyoshi, H., Kanaya, Y., Zhu, C., and Taketani, F.: Tagged tracer simulations of black
533 carbon in the Arctic: transport, source contributions, and budget, *Atmos. Chem. Phys.*, 17, 10515–10533,
534 <https://doi.org/10.5194/acp-17-10515-2017>, 2017.

535 IPCC: Climate change 2021: the physical science basis, edited by: Masson-Delmotte, V., Zhai, P., Pirani, A., Connors, S. L.,
536 Péan, C., Berger, S., Caud, N., Chen, Y., Goldfarb, L., Gomis, M. I., and Others, Cambridge University Press Cambridge, UK,
537 2021.

538 Kanaya, Y., Komazaki, Y., Pochanart, P., Liu, Y., Akimoto, H., Gao, J., Wang, T., and Wang, Z.: Mass concentrations of
539 black carbon measured by four instruments in the middle of Central East China in June 2006, *Atmos. Chem. Phys.*, 8, 7637–
540 7649, <https://doi.org/10.5194/acp-8-7637-2008>, 2008.

541 Kanaya, Y., Pan, X., Miyakawa, T., Komazaki, Y., Taketani, F., Uno, I., and Kondo, Y.: Long-term observations of black
542 carbon mass concentrations at Fukue Island, western Japan, during 2009–2015: constraining wet removal rates and emission
543 strengths from East Asia, *Atmos. Chem. Phys.*, 16, 10689–10705, <https://doi.org/10.5194/acp-16-10689-2016>, 2016.

544 Kanaya, Y., Yamaji, K., and Miyakawa, T.: Rapid reduction in black carbon emissions from China: evidence from 2009–2019
545 observations on Fukue Island, Japan, *Atmos. Chem. Phys.*, <https://doi.org/10.5194/acp-20-6339-2020>, 2020.

546 Kaplan, J. O. and Lau, K. H.-K.: The WGLC global gridded lightning climatology and time series, *Earth Syst. Sci. Data*, 13,
547 3219–3237, <https://doi.org/10.5194/essd-13-3219-2021>, 2021.

548 Kasai, Y. J., Koshiro, T., Endo, M., Jones, N. B., and Murayama, Y.: Ground-based measurement of strato–mesospheric CO
549 by a FTIR spectrometer over Poker Flat, Alaska, *Adv. Space Res.*, 35, 2024–2030, <https://doi.org/10.1016/j.asr.2005.04.099>,
550 2005.

551 Kim, Y., Hatsushika, H., Muskett, R. R., and Yamazaki, K.: Possible effect of boreal wildfire soot on Arctic sea ice and Alaska
552 glaciers, *Atmos. Environ.*, 39, 3513–3520, <https://doi.org/10.1016/j.atmosenv.2005.02.050>, 2005.

- 553 Klimont, Z., Kupiainen, K., Heyes, C., Purohit, P., Cofala, J., Rafaj, P., Borken-Kleefeld, J., and Schöpp, W.: Global
554 anthropogenic emissions of particulate matter including black carbon, *Atmos. Chem. Phys.*, 17, 8681–8723,
555 <https://doi.org/10.5194/acp-17-8681-2017>, 2017.
- 556 Kondo, Y., Sahu, L., Kuwata, M., Miyazaki, Y., Takegawa, N., Moteki, N., Imaru, J., Han, S., Nakayama, T., Oanh, N. T. K.,
557 Hu, M., Kim, Y. J., and Kita, K.: Stabilization of the Mass Absorption Cross Section of Black Carbon for Filter-Based
558 Absorption Photometry by the use of a Heated Inlet, *Aerosol Sci. Technol.*, 43, 741–756,
559 <https://doi.org/10.1080/02786820902889879>, 2009.
- 560 Kondo, Y., Sahu, L., Moteki, N., Khan, F., Takegawa, N., Liu, X., Koike, M., and Miyakawa, T.: Consistency and traceability
561 of black carbon measurements made by laser-induced incandescence, thermal-optical transmittance, and filter-based photo-
562 absorption techniques, *Aerosol Sci. Technol.*, 45, 295–312, <https://doi.org/10.1080/02786826.2010.533215>, 2011a.
- 563 Kondo, Y., Matsui, H., Moteki, N., Sahu, L., Takegawa, N., Kajino, M., Zhao, Y., Cubison, M. J., Jimenez, J. L., Vay, S.,
564 Diskin, G. S., Anderson, B., Wisthaler, A., Mikoviny, T., Fuelberg, H. E., Blake, D. R., Huey, G., Weinheimer, A. J., Knapp,
565 D. J., and Brune, W. H.: Emissions of black carbon, organic, and inorganic aerosols from biomass burning in North America
566 and Asia in 2008, *J. Geophys. Res.*, 116, <https://doi.org/10.1029/2010jd015152>, 2011b.
- 567 Li, F., Zhang, X., Kondragunta, S., and Csizsar, I.: Comparison of fire radiative power estimates from VIIRS and MODIS
568 observations, *J. Geophys. Res.*, 123, 4545–4563, <https://doi.org/10.1029/2017jd027823>, 2018.
- 569 Lund, M. T., Samset, B. H., Skeie, R. B., Watson-Parris, D., Katich, J. M., Schwarz, J. P., and Weinzierl, B.: Short Black
570 Carbon lifetime inferred from a global set of aircraft observations, *npj Climate and Atmospheric Science*, 1, 1–8,
571 <https://doi.org/10.1038/s41612-018-0040-x>, 2018.
- 572 Matsui, H., Mori, T., Ohata, S., Moteki, N., Oshima, N., Goto-Azuma, K., Koike, M., and Kondo, Y.: Contrasting source
573 contributions of Arctic black carbon to atmospheric concentrations, deposition flux, and atmospheric and snow radiative effects,
574 *Atmos. Chem. Phys.*, 22, 8989–9009, <https://doi.org/10.5194/acp-22-8989-2022>, 2022.
- 575 Miyazaki, Y., Kondo, Y., Sahu, L. K., Imaru, J., Fukushima, N., and Kano, M.: Performance of a newly designed continuous
576 soot monitoring system (COSMOS), *J. Environ. Monit.*, 10, 1195–1201, <https://doi.org/10.1039/b806957c>, 2008.
- 577 Mori, T., Kondo, Y., Ohata, S., Zhao, Y., Sinha, P. R., Oshima, N., Matsui, H., Moteki, N., and Koike, M.: Seasonal variation
578 of wet deposition of black carbon in arctic Alaska, *J. Geophys. Res.*, 125, <https://doi.org/10.1029/2019jd032240>, 2020.
- 579 Mouteva, G. O., Czimczik, C. I., Fahrni, S. M., Wiggins, E. B., Rogers, B. M., Veraverbeke, S., Xu, X., Santos, G. M.,
580 Henderson, J., Miller, C. E., and Randerson, J. T.: Black carbon aerosol dynamics and isotopic composition in Alaska linked
581 with boreal fire emissions and depth of burn in organic soils, *Global Biogeochem. Cycles*, 29, 1977–2000,
582 <https://doi.org/10.1002/2015gb005247>, 2015.
- 583 Ohata, S., Mori, T., Kondo, Y., Sharma, S., Hyvärinen, A., Andrews, E., Tunved, P., Asmi, E., Backman, J., Servomaa, H.,
584 and Others: Estimates of mass absorption cross sections of black carbon for filter-based absorption photometers in the Arctic,
585 *Atmos. Meas. Tech.*, 14, 6723–6748, <https://doi.org/10.5194/amt-14-6723-2021>, 2021.
- 586 Oshima, N., Yukimoto, S., Deushi, M., Koshiro, T., Kawai, H., Tanaka, T. Y., and Yoshida, K.: Global and Arctic effective
587 radiative forcing of anthropogenic gases and aerosols in MRI-ESM2.0, *Prog. Earth Planet. Sci.*, 7, 38,
588 <https://doi.org/10.1186/s40645-020-00348-w>, 2020.
- 589 Overland, J. E., Wang, M., Walsh, J. E., and Stroeve, J. C.: Future Arctic climate changes: Adaptation and mitigation time
590 scales, *Earths Future*, 2, 68–74, <https://doi.org/10.1002/2013ef000162>, 2014.

591 Pan, X., Kanaya, Y., Taketani, F., Miyakawa, T., Inomata, S., Komazaki, Y., Tanimoto, H., Wang, Z., Uno, I., and Wang, Z.:
592 Emission characteristics of refractory black carbon aerosols from fresh biomass burning: a perspective from laboratory
593 experiments, *Atmos. Chem. Phys.*, 17, 13001–13016, <https://doi.org/10.5194/acp-17-13001-2017>, 2017.

594 Pan, X., Ichoku, C., Chin, M., Bian, H., Darmenov, A., Colarco, P., Ellison, L., Kucsera, T., da Silva, A., Wang, J., Oda, T.,
595 and Cui, G.: Six global biomass burning emission datasets: intercomparison and application in one global aerosol model,
596 *Atmos. Chem. Phys.*, 20, 969–994, <https://doi.org/10.5194/acp-20-969-2020>, 2020.

597 Paris, J.-D., Stohl, A., Nédélec, P., Arshinov, M. Y., Panchenko, M. V., Shmargunov, V. P., Law, K. S., Belan, B. D., and
598 Ciais, P.: Wildfire smoke in the Siberian Arctic in summer: source characterization and plume evolution from airborne
599 measurements, *Atmos. Chem. Phys.*, 9, 9315–9327, <https://doi.org/10.5194/acp-9-9315-2009>, 2009.

600 Picotte, J. J., Bhattarai, K., Howard, D., Lecker, J., Epting, J., Quayle, B., Benson, N., and Nelson, K.: Changes to the
601 Monitoring Trends in Burn Severity program mapping production procedures and data products, *Fire Ecology*, 16, 16,
602 <https://doi.org/10.1186/s42408-020-00076-y>, 2020.

603 Polissar, A. V., Hopke, P. K., Malm, W. C., and Sisler, J. F.: The ratio of aerosol optical absorption coefficients to sulfur
604 concentrations, as an indicator of smoke from forest fires when sampling in polar regions, *Atmos. Environ.*, 30, 1147–1157,
605 [https://doi.org/10.1016/1352-2310\(95\)00334-7](https://doi.org/10.1016/1352-2310(95)00334-7), 1996.

606 Polissar, A. V., Hopke, P. K., and Malm, W. C.: Atmospheric aerosol over Alaska: 1. Spatial and seasonal variability, *J.*
607 *Geophys. Res.*, <https://doi.org/10.1029/98JD01365>, 1998.

608 Quinn, P. K., Shaw, G., Andrews, E., Dutton, E. G., Ruoho-Airola, T., and Gong, S. L.: Arctic haze: current trends and
609 knowledge gaps, *Tellus B Chem. Phys. Meteorol.*, 59, 99, <https://doi.org/10.1111/j.1600-0889.2006.00236.x>, 2007.

610 Reap, R. M.: Climatological Characteristics and Objective Prediction of Thunderstorms over Alaska, *Weather Forecast.*, 6,
611 309–319, [https://doi.org/10.1175/1520-0434\(1991\)006<0309:CCAOPO>2.0.CO;2](https://doi.org/10.1175/1520-0434(1991)006<0309:CCAOPO>2.0.CO;2), 1991.

612 Rogers, H. M., Ditto, J. C., and Gentner, D.: Evidence for impacts on surface-level air quality in the northeastern US from
613 long-distance transport of smoke from North American fires during the Long Island Sound Tropospheric Ozone Study
614 (LISTOS) 2018, *Atmos. Chem. Phys.*, 20, 671–682, <https://doi.org/10.5194/acp-20-671-2020>, 2020.

615 Sauvage, B., Fontaine, A., Eckhardt, S., Auby, A., Boulanger, D., Petetin, H., Paugam, R., Athier, G., Cousin, J.-M., Darras,
616 S., and Others: Source attribution using FLEXPART and carbon monoxide emission inventories: SOFT-IO version 1.0, *Atmos.*
617 *Chem. Phys.*, 17, 15271–15292, <https://doi.org/10.5194/acp-17-15271-2017>, 2017.

618 Schmale, J., Arnold, S. R., Law, K. S., and Thorp, T.: Local Arctic air pollution: A neglected but serious problem, *Earth's*
619 *Future*, <https://doi.org/10.1029/2018EF000952>, 2018.

620 Schmale, J., Zieger, P., and Ekman, A. M. L.: Aerosols in current and future Arctic climate, *Nat. Clim. Chang.*, 11, 95–105,
621 <https://doi.org/10.1038/s41558-020-00969-5>, 2021.

622 Selimovic, V., Yokelson, R. J., Warneke, C., Roberts, J. M., de Gouw, J., Reardon, J., and Griffith, D. W. T.: Aerosol optical
623 properties and trace gas emissions by PAX and OP-FTIR for laboratory-simulated western US wildfires during FIREX, *Atmos.*
624 *Chem. Phys.*, 18, 2929–2948, <https://doi.org/10.5194/acp-18-2929-2018>, 2018.

625 Selimovic, V., Yokelson, R. J., McMeeking, G. R., and Coefield, S.: In situ measurements of trace gases, PM, and aerosol
626 optical properties during the 2017 NW US wildfire smoke event, *Atmos. Chem. Phys.*, 19, 3905–3926,
627 <https://doi.org/10.5194/acp-19-3905-2019>, 2019.

- 628 Sharma, S., Ishizawa, M., Chan, D., Lavoué, D., Andrews, E., Eleftheriadis, K., and Maksyutov, S.: 16-year simulation of
629 Arctic black carbon: Transport, source contribution, and sensitivity analysis on deposition, *J. Geophys. Res.*, 118, 943–964,
630 <https://doi.org/10.1029/2012jd017774>, 2013.
- 631 Sierra-Hernández, M. R., Beaudon, E., Porter, S. E., Mosley-Thompson, E., and Thompson, L. G.: Increased fire activity in
632 Alaska since the 1980s: Evidence from an ice core-derived black carbon record, *J. Geophys. Res.*, 127,
633 <https://doi.org/10.1029/2021jd035668>, 2022.
- 634 Sinha, P. R., Kondo, Y., Koike, M., Ogren, J. A., Jefferson, A., Barrett, T. E., Sheesley, R. J., Ohata, S., Moteki, N., Coe, H.,
635 Liu, D., Irwin, M., Tunved, P., Quinn, P. K., and Zhao, Y.: Evaluation of ground-based black carbon measurements by filter-
636 based photometers at two Arctic sites, *J. Geophys. Res.*, 122, 3544–3572, <https://doi.org/10.1002/2016jd025843>, 2017.
- 637 Skamarock, W. C., Klemp, J. B., Dudhia, J., Gill, D. O., Liu, Z., Berner, J., Wang, W., Powers, J. G., Duda, M. G., Barker, D.
638 M., and Others: A description of the advanced research WRF model version 4, National Center for Atmospheric Research:
639 Boulder, CO, USA, 145, 2019.
- 640 Stein, A. F., Draxler, R. R., Rolph, G. D., Stunder, B. J. B., Cohen, M. D., and Ngan, F.: NOAA’s HYSPPLIT Atmospheric
641 Transport and Dispersion Modeling System, *Bull. Am. Meteorol. Soc.*, 96, 2059–2077, <https://doi.org/10.1175/BAMS-D-14-00110.1>, 2015.
- 643 Stohl, A., Andrews, E., Burkhardt, J. F., Forster, C., Herber, A., Hoch, S. W., Kowal, D., Lunder, C., Mefford, T., Ogren, J. A.,
644 Sharma, S., Spichtinger, N., Stebel, K., Stone, R., Ström, J., Tørseth, K., Wehrli, C., and Yttri, K. E.: Pan-Arctic enhancements
645 of light absorbing aerosol concentrations due to North American boreal forest fires during summer 2004, *J. Geophys. Res.*,
646 111, <https://doi.org/10.1029/2006jd007216>, 2006.
- 647 Taketani, F., Miyakawa, T., Takashima, H., Komazaki, Y., Pan, X., Kanaya, Y., and Inoue, J.: Shipborne observations of
648 atmospheric black carbon aerosol particles over the Arctic Ocean, Bering Sea, and North Pacific Ocean during September
649 2014, *J. Geophys. Res.*, 121, 1914–1921, <https://doi.org/10.1002/2015jd023648>, 2016.
- 650 Taketani, F., Miyakawa, T., Takigawa, M., Yamaguchi, M., Komazaki, Y., Mordovskoi, P., Takashima, H., Zhu, C., Nishino,
651 S., Tohjima, Y., and Others: Characteristics of atmospheric black carbon and other aerosol particles over the Arctic Ocean in
652 early autumn 2016: Influence from biomass burning as assessed with observed microphysical properties and model simulations,
653 *Sci. Total Environ.*, 848, 157671, <https://doi.org/10.1016/j.scitotenv.2022.157671>, 2022.
- 654 Thackeray, C. W. and Hall, A.: An emergent constraint on future Arctic sea-ice albedo feedback, *Nat. Clim. Chang.*, 9, 972–
655 978, <https://doi.org/10.1038/s41558-019-0619-1>, 2019.
- 656 Vasileva, Moiseenko, and Skorokhod: Emission ratios of trace gases and particles for Siberian forest fires on the basis of
657 mobile ground observations, *Atmos. Chem. Phys.*, <https://doi.org/10.5194/acp-17-12303-2017>, 2017.
- 658 Wang, H., Rasch, P. J., Easter, R. C., Singh, B., Zhang, R., Ma, P.-L., Qian, Y., Ghan, S. J., and Beagley, N.: Using an explicit
659 emission tagging method in global modeling of source-receptor relationships for black carbon in the Arctic: Variations, sources,
660 and transport pathways, *J. Geophys. Res.*, 119, 12,888–12,909, <https://doi.org/10.1002/2014jd022297>, 2014.
- 661 Wang, Q., Jacob, D. J., Fisher, J. A., Mao, J., Leibensperger, E. M., Carouge, C. C., Le Sager, P., Kondo, Y., Jimenez, J. L.,
662 Cubison, M. J., and Doherty, S. J.: Sources of carbonaceous aerosols and deposited black carbon in the Arctic in winter-spring:
663 implications for radiative forcing, *Atmos. Chem. Phys.*, 11, 12453–12473, <https://doi.org/10.5194/acp-11-12453-2011>, 2011.

- 664 van der Werf, G. R., Randerson, J. T., Giglio, L., van Leeuwen, T. T., Chen, Y., Rogers, B. M., Mu, M., van Marle, M. J. E.,
665 Morton, D. C., Collatz, G. J., Yokelson, R. J., and Kasibhatla, P. S.: Global fire emissions estimates during 1997–2016, *Earth*
666 *Syst. Sci. Data*, 9, 697–720, <https://doi.org/10.5194/essd-9-697-2017>, 2017.
- 667 van der Werf, G., Randerson, J. T., Giglio, L., Chen, Y., Rogers, B. M., and Van Leeuwen, T. T.: Global Fire Emissions
668 Database version 4 (GFED4), GC33D-0545, 2014.
- 669 Whaley, C. H., Mahmood, R., von Salzen, K., Winter, B., Eckhardt, S., Arnold, S., Beagley, S., Becagli, S., Chien, R.-Y.,
670 Christensen, J., and Others: Model evaluation of short-lived climate forcers for the Arctic Monitoring and Assessment
671 Programme: a multi-species, multi-model study, *Atmos. Chem. Phys.*, 22, 5775–5828, [https://doi.org/10.5194/acp-22-5775-](https://doi.org/10.5194/acp-22-5775-2022)
672 [2022](https://doi.org/10.5194/acp-22-5775-2022), 2022.
- 673 Wiggins, E. B., Soja, A. J., Gargulinski, E., Halliday, H. S., Pierce, R. B., Schmidt, C. C., Nowak, J. B., DiGangi, J. P., Diskin,
674 G. S., Katich, J. M., Perring, A. E., Schwarz, J. P., Anderson, B. E., Chen, G., Crosbie, E. C., Jordan, C., Robinson, C. E.,
675 Sanchez, K. J., Shingler, T. J., Shook, M., Thornhill, K. L., Winstead, E. L., Ziemba, L. D., and Moore, R. H.: High temporal
676 resolution satellite observations of fire radiative power reveal link between fire behavior and aerosol and gas emissions,
677 *Geophys. Res. Lett.*, 47, <https://doi.org/10.1029/2020gl090707>, 2020.
- 678 Xie, A., Zhu, J., Kang, S., Qin, X., Xu, B., and Wang, Y.: Polar amplification comparison among Earth’s three poles under
679 different socioeconomic scenarios from CMIP6 surface air temperature, *Sci. Rep.*, 12, 16548, [https://doi.org/10.1038/s41598-](https://doi.org/10.1038/s41598-022-21060-3)
680 [022-21060-3](https://doi.org/10.1038/s41598-022-21060-3), 2022.
- 681 Xu, J.-W., Martin, R. V., Morrow, A., Sharma, S., Huang, L., Leaitch, W. R., Burkart, J., Schulz, H., Zanatta, M., Willis, M.
682 D., Henze, D. K., Lee, C. J., Herber, A. B., and Abbatt, J. P. D.: Source attribution of Arctic black carbon constrained by
683 aircraft and surface measurements, *Atmos. Chem. Phys.*, 17, 11971–11989, <https://doi.org/10.5194/acp-17-11971-2017>, 2017.
- 684 Yurganov, L. N., Jaffe, D. A., Pullman, E., and Novelli, P. C.: Total column and surface densities of atmospheric carbon
685 monoxide in Alaska, 1995, *J. Geophys. Res.*, 103, 19337–19345, <https://doi.org/10.1029/97jd02299>, 1998.
- 686 Zheng, B., Ciais, P., Chevallier, F., Yang, H., Canadell, J. G., Chen, Y., van der Velde, I. R., Aben, I., Chuvieco, E., Davis, S.
687 J., Deeter, M., Hong, C., Kong, Y., Li, H., Li, H., Lin, X., He, K., and Zhang, Q.: Record-high CO₂ emissions from boreal
688 fires in 2021, *Science*, 379, 912–917, <https://doi.org/10.1126/science.ade0805>, 2023.
- 689 Zhu, C., Kanaya, Y., Takigawa, M., Ikeda, K., Tanimoto, H., Taketani, F., Miyakawa, T., Kobayashi, H., and Pisso, I.:
690 FLEXPART v10.1 simulation of source contributions to Arctic black carbon, *Atmos. Chem. Phys.*, 20, 1641–1656,
691 <https://doi.org/10.5194/acp-20-1641-2020>, 2020.
- 692